Materials Today Advances 12 (2021) 100170

Contents lists available at ScienceDirect

Materials Today Advances

journal homepage: www.journals.elsevier.com/materials-today-advances/

Mid-infrared modulators integrating silicon and black phosphorus photonics

L. Huang [a, d], B. Dong [a, d], Z.G. Yu [c], J. Zhou [a], Y. Ma [a], Y.-W. Zhang [c], C. Lee [a, **], K.-W. Ang [a, b, *]

[a] Department of Electrical and Computer Engineering, National University of Singapore, 4 Engineering Drive 3, 117583, Singapore
[b] Institute of Materials Research and Engineering, A*STAR, 2 Fusionopolis Way, 138634, Singapore
[c] Institute for High Performance Computing, A*STAR, 1 Fusionopolis Way, 138632, Singapore

A R T I C L E I N F O

Article history:
Received 30 July 2021
Received in revised form 30 August 2021
Accepted 2 September 2021
Available online xxx

Keywords:
Black phosphorus
Modulator
Photodetector
Mid-infrared
Silicon photonics
On-chip integration

A B S T R A C T

Vast applications of mid-infrared await the realisation of integrated photonic systems for this unique spectrum. Despite its potential as a universal platform for diverse active functions in mid-infrared, black phosphorus (BP) photonics still lacks integrated modulators for completion. Here we realize a hybrid integration of mid-infrared BP modulator on silicon photonics waveguide. Through gating effect, the anisotropic absorption in armchair BP can be tuned for enabling efficient optical modulation spanning ~3.85–4.1 μm. The integrated waveguide design further promotes light–BP interaction that achieves a modulation depth of ~5 dB at a low bias of −4 V. Additionally, the active footprint of 225 μm^2 and the switching energy of ~2.6 pJ are remarkably smaller compared to traditional counterparts. Function diversity of such a platform is further verified by integrating BP photodetector and modulator. The combination of two-dimensional materials and silicon photonics manifests a versatile platform to realise high-performance optoelectronic devices for compact on-chip mid-infrared system.

1. Introduction

Despite numerous potential applications in mid-infrared such as gas sensing, medical diagnostics, night vision and food quality inspection [1–3], chip-scale mid-infrared system has not been realised yet primarily due to the material's incompatibility issue between passive and active photonic components. Although the passive functions such as guiding and coupling of light could still be fulfilled within the silicon platform, the active building blocks such as photodetectors, modulators and lasers usually require the deployment of several different materials. Electro-optic modulators are one of the essential active components in photonic circuits and could be employed for applications such as to increase signal-to-noise ratio for sensing [4], to generate binary digits for computing and data communication [5] and to steer light beam for light detection and ranging [6]. So far, the technology for mid-infrared optical modulators is still under development with limited progress, which remains a bottleneck for realising on-chip mid-infrared systems (Fig. 1a).

To date, there are only a few works on waveguide-integrated optical modulators for mid-infrared, which operate based on the Pockels effect in lithium niobite, thermo-optic effect and free carrier effect in silicon and germanium [7–12]. The dimensions of these modulator are in the scale of millimetres, hindering the realisation of compact photonic systems. Moreover, the active materials for light modulation in the existing works could not provide potential solutions to other active functions such as photodetection and lasing in mid-infrared, which means another set of materials are still needed in order to complete the whole system. This may lead to extra complexity in fabrication and high cost of manufacturing.

Black phosphorus (BP), a member of the two-dimensional (2D) materials family, shows versatile potential for different active functions in mid-infrared systems, from photodetection to light modulation and lasing [13–22]. Besides function diversity, compatibility with various substrates [23,24], polarisation sensitivity [25] and tuneable narrow bandgap [17] distinguish BP from the other candidates for mid-infrared optoelectronics. So far,

* Corresponding author.
** Corresponding author.
E-mail addresses: elelc@nus.edu.sg (C. Lee), eleakw@nus.edu.sg (K.-W. Ang).
[d] Co-first authors.

https://doi.org/10.1016/j.mtadv.2021.100170

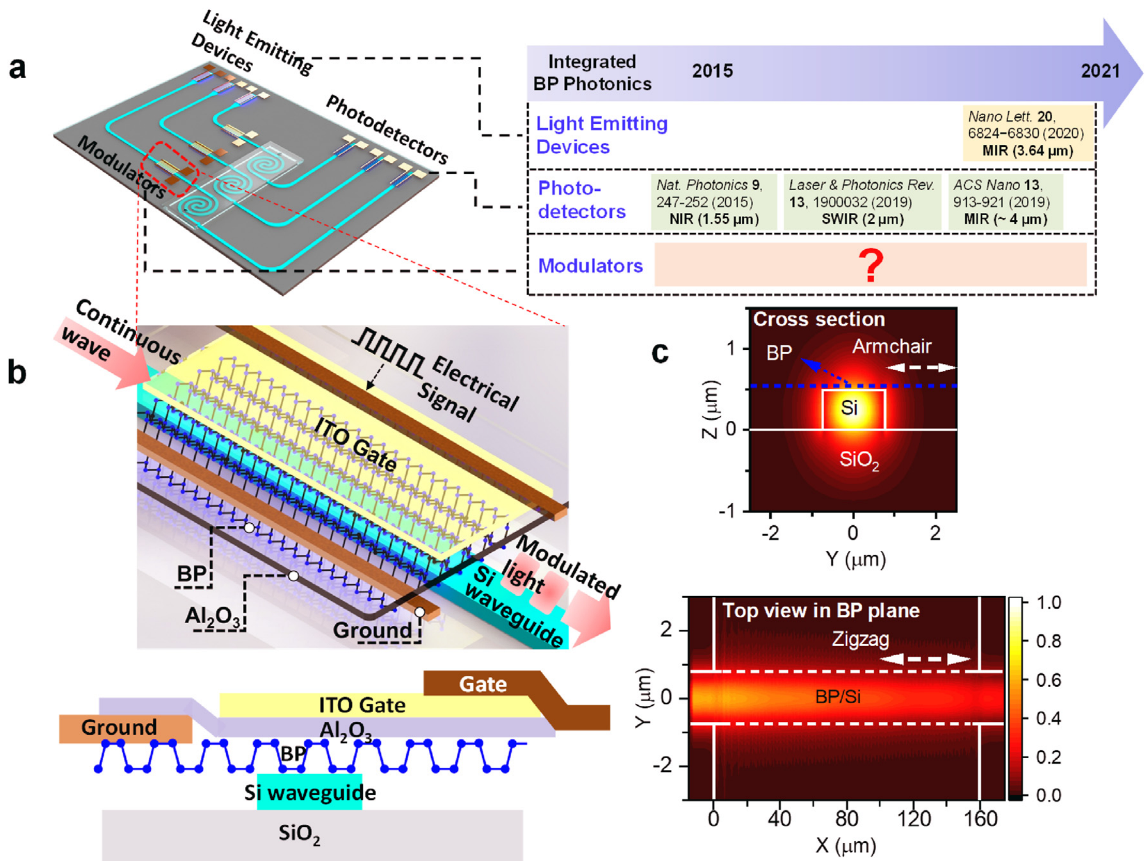

Fig. 1. (a) Light emission, modulation and detection are the essential active functions in a mid-infrared system. Although integrated photodetectors and light emitting diodes have been demonstrated in this work, we realise the missing critical building block of modulator. (b) Optical modulation is enabled by applying a vertical electrical field to BP, which interacts with the propagating mid-infrared wave in the Si waveguide underneath. Cross section is perpendicular to light propagation direction. (c) Light is absorbed by BP while propagating along the Si waveguide (bottom) in its core region (top).

integration efforts have been made on BP photodetectors [14,26,27] and light-emitting devices [28] (Fig. 1a). Theoretical studies [29,30] have predicted that the optical properties of thin-film BP could be effectively modulated by applying a vertical electric field, as verified by experimental observations [15,31–35]. Despite the promising prospects foreseen by the fundamental studies, an integrated BP electro-optic modulator has not been demonstrated yet. Completing the missing part of modulators would be a significant step towards exploiting BP to its full potential.

Here we realise a waveguide-integrated electro-optic modulator for a mid-infrared wavelength range up to 4.1 μm. The hybrid system, featuring the integration of 2D BP and Si photonics, takes advantage of the well-established Si fabrication technology as well as the unique properties of BP to meet the requirements in mid-infrared. To guide the design of our BP modulator, we first investigated the polarisation-resolved Fourier transform infrared (FTIR) spectra of a surface-illuminated sample with gating effect. Refractive index and extinction coefficient of BP were extracted and design guidelines in terms of waveguide propagation mode, operation wavelength and alignment of BP crystal orientation are presented. We then realised the waveguide-integrated BP modulator for a spectral range from 3.85 to 4.1 μm. Modulation mechanisms were analysed using gate voltage (V_g)-dependent time response of the modulated light signal under different modulation frequencies, and verified by theoretical calculations. Modulation depth under varying illumination power was also investigated and analysed using a saturable absorption model. Finally, we will show our efforts in integrating the two active components of photodetector and modulator on the same chip as a step towards all-BP photonics, and discuss the challenges and our perspectives for future work.

2. Results and discussion

The integrated modulator consists of an ITO (indium tin oxide)-Al_2O_3 (aluminium oxide)-BP capacitor on top of the silicon waveguide (Fig. 1b). The propagating light in the Si photonics waveguide interacts with BP and its intensity is modulated by the absorption change in BP (Fig. 1c) when gate bias is switched between different levels. Details of the Si photonic layer characterisations and the active BP layer structures are shown in Supporting Note 1. Analysis of light distribution and propagation is provided in Supporting Note 2. In order to quantitatively analyse the light–BP interaction and its gate modulation, we began with the characterisation of a surface-illuminated sample (Supporting Note 3) using FTIR spectroscopy. When the light is polarised along the armchair orientation of BP, the absorption by BP is much stronger than that along the zigzag direction (Fig. 2a). The absorption shows a steep roll-off after 3.5 μm and is cut off at 4.2 μm, corresponding to a bandgap of 0.295 eV. With the light source polarised along the armchair orientation, we then measured the absorption change in BP by applying varying gate biases (V_g) (Fig. 2b). The absorption change (modulation strength) caused by V_g is defined as follows: $\Delta Absorption = \frac{absorbed\ power}{incident\ power}|_{V_g \neq 0V} - \frac{absorbed\ power}{incident\ power}|_{V_g = 0V}$. Positive V_g shifts the fermi level up towards conduction band, narrowing the effective bandgap of BP, and results in an increased absorption. On

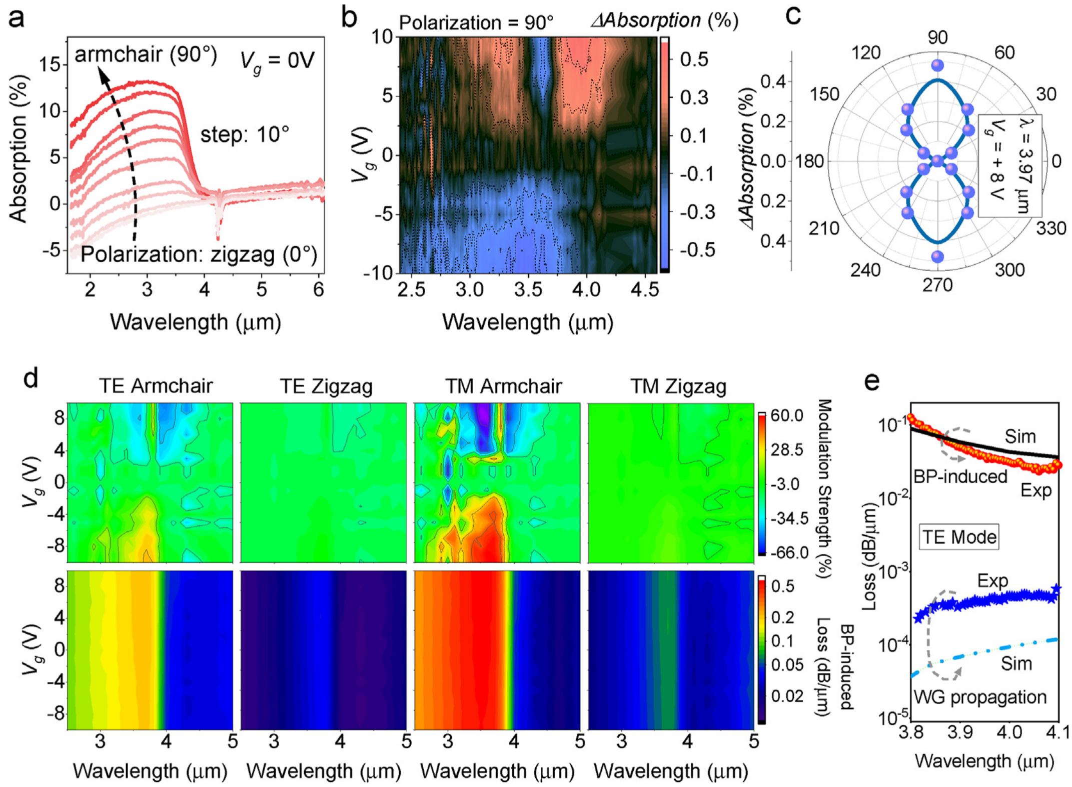

Fig. 2. (a) Absorption in BP gradually increases as light polarisation is rotated from zigzag to armchair. (b) The gate modulation is effective near the absorption edge of BP and (c) only for polarisation along armchair orientation. (d) Simulated V_g wavelength mapping of the modulation strength (upper row, interaction length: 150 μm) and BP-induced loss (lower row) for TE and TM modes with different BP crystal orientation. Effective modulation and moderate loss could be obtained when the waveguide is operated in TE mode with BP's armchair aligned with the transverse direction. Modulation strength is significantly enhanced by the waveguide integration compared to the surface-illuminated case in (b). (e) Spectral waveguide propagation loss and BP-induced loss indicate good agreement between simulations (Sim) and experiment (Exp).

the other hand, negative V_g broadens the effective bandgap as more holes are filling up the valence band, and absorption of BP is reduced as a result. With 10 V gate bias, a ΔAbsorption of ~0.5% could be induced at the characteristic wavelengths. These characteristic wavelengths and their oscillations (at the peaks and valleys) might be caused by the sub-band transitions in BP [15,30]. The gate modulation is effective mainly for the wavelength between 3 and 4.5 μm, near the absorption edge of BP. The operational wavelength could be tuned by BP thickness, using b-AsP alloy [36] or applying a vertical DC (direct current) bias [32], so as to cover a broad spectrum for a wide range of applications. Next, we investigated the absorption change with different light polarisations under a fixed V_g of°±°8°V (Fig. S3-6). When the incident light is polarised along the zigzag orientation (0°) of BP, no modulation signal was observed. As the polarisation gradually rotates towards the armchair orientation, the modulation signal starts to appear with its amplitude monotonously increasing and peaks when the light is polarised along the armchair direction. The phenomenon is featured in the polar plot (Fig. 2c) for the case of $V_g = 8$ V at a characteristic wavelength of 3.97 μm. This indicates that light polarised along zigzag orientation is not subject to gate bias and only light with polarisation along armchair orientation could contribute to the modulation.

In the FTIR measurement of the surface-illuminated sample, the modulation strength is less than 1%, which may not be efficient enough for practical applications. By implementing waveguide integration, we could expect an enhancement of the modulation strength compared to the free space case. To investigate the light–BP interaction in the waveguide-integrated modulator and provide a guideline for its design and operation, we performed simulations based on the extracted n (refractive index) and k (extinction coefficient) of BP from the FTIR spectra under varying V_g using transfer matrix method (Supporting Note 4). The strong anisotropy of the n and k (Fig. S4-2) implies that the alignment of BP's crystal orientation and the propagation mode in the waveguide will be critical to the modulator performance. The refractive index along the armchair orientation of BP is larger than the refractive index of Si (~3.43), which is conducive to the interaction between BP and the guided wave in Si. For TM (transverse magnetic) mode, the E-field is mainly distributed at the top and bottom boundaries of the Si waveguide, while for TE (transverse electric) mode the E-field is mainly confined within the core of the Si waveguide (Fig. S2-1). Therefore, higher modulation strength (Fig. 2d, upper row) could be obtained with TM mode when the armchair orientation of BP is aligned with E_x, at the expense of a higher BP-induced loss (Fig. 2d, lower row). When the waveguide is operated under TE mode with the armchair orientation aligned with E_y, we could expect a moderate BP-induced loss, with a lower yet still effective modulation. The modulation strength is enhanced by the waveguide integration (compare Fig. 2b and d), from ~0.5% in the surface-illuminated case to ~27% over 150-μm light–BP interaction length (at 4 μm, 10 V, TE Armchair). In surface illumination cases, light propagation in free space only allows for a transient light–BP interaction limited by the small thickness of BP. The enhancement from waveguide integration is enabled by the on-chip propagation of light which is well-confined around the space occupied by BP. The interaction length is therefore increased from nanometre to micron scale, accounting for the significantly strengthened modulation. The measured waveguide propagation loss is higher than simulation result due to fabrication imperfections such as side wall roughness and dimension shift, while for BP-induced loss the measurement agrees well with the simulation (Fig. 2e). With the presence of BP, the mode in the Si waveguide is coupled up into BP due to the higher refractive index of BP, as revealed by the comparison in Fig. S2-2. TM mode suffers from higher BP-induced loss as a result of more overlap between the propagation mode and BP. In addition, TM mode also undergoes a more severe leakage into the substrate and along the fins of SWG (sub-wavelength grating) (Fig. S2-3). On the contrary, TE mode is much less lossy due to better mode confinement.

Based on the FTIR and simulation results, we chose to operate the integrated Si-BP modulator at wavelengths near BP's absorption edge, and in TE mode with the armchair orientation of BP aligned to the transverse direction of the waveguide. For the BP layer (Fig. S1-3b), we chose a thickness of 20 nm for a better gate control over the channel, meanwhile maintaining a narrow bandgap for mid-infrared wavelengths [30,32]. For a start, we fixed the wavelength at 4 μm and measured the time response of the modulated signal. Here we adopted three different ways for applying V_g signal: square waves (50% duty cycle) with 4 V peak-to-peak amplitude and −2 V, 0 V and +2 V offset respectively (Fig. 3a), which correspond to different doping conditions in BP. With negative V_g, light absorption by BP decreases and consequently the intensity of light signal increases. On the contrary, light attenuates with positive V_g as BP on the waveguide creates higher extinction. The higher and lower transmission of light represents the binary '1' state (or on state) and the binary '0' state (or off state) of the modulator, respectively. The modulated signal is a manifestation of the bandgap tuned by gating effect through a combination of the Burstein−Moss effect [37] and the Franz−Keldysh effect [38]. The Burstein−Moss effect is the change in effective bandgap (Fig. 3b) due to band filling as V_g tunes the Fermi level (Fig. S5-2a), while the Franz−Keldysh effect is the reduction in bandgap (Fig. 3c) induced by the shift of valence band maximum and conduction band minimum under an external vertical electric field (Fig.S5-2b). The BP flake is initially heavily p-doped (Fig. 3b at $V_g = 0$ V). With negative V_g, the Fermi level of BP shifts further below the valence band maximum and leads to a larger effective bandgap (>0.3 eV). This explains the higher transmission of light under negative V_g in Fig. 3a. Weaker modulation is presented in the positive V_g regime, as V_g crosses the charge neutral point into the lightly *n*-doped condition (Supporting Note 6 at $V_g = 4$ V), resulting in a weakening of the Burstein−Moss effect. On the other hand, in the Franz−Keldysh effect the conduction band minimum shifts faster than the valence band maximum as the electric field is increased, narrowing the bandgap as a result (Fig. 3c). However, due to the small V_g applied in our measurement, the induced vertical electric field is too small to cause any substantial change in the bandgap. Consequently, the modulation mechanism in our device is dominated by Burstein−Moss effect. The anisotropic optical modulation in BP is also verified by the DFT calculations. The optical conductivity along armchair orientation (σ_{xx}) (Fig. S5-2c) could be effectively modulated while along zigzag orientation the optical conductivity (σ_{yy}) (Fig. S5-2d) is not responsive to external electric field.

To evaluate the effectiveness of the modulation, modulation depth is defined as *Modulation depth* $(dB) = 10\log\frac{P_0}{P_1}$, where P_0 is the transmitted light power for the '0' state and P_1 is the transmitted light power for the '1' state. Modulation depth describes how much extinction could be created by the V_g for the two states. The modulation depth gradually decreases as the wavelength is increased from 3.85 to 4.05 μm (Fig. 3d and e). Larger amplitude of the AC (alternating current) V_g signal leads to more pronounced change in effective bandgap, resulting in higher modulation depth. Similar to the strongly power-dependent responsivity of BP photodetectors due to saturable absorption, we could also observe a noticeable increase in the modulation depth as the light gets weaker (Fig. 4a and b). A modulation depth of ~5 dB is achieved at 3.85 μm under 120 μW power and −4 V gate bias. A higher modulation depth could be expected by further decreasing the power, as the trend exhibits no signs of saturation yet. The extinction coefficient (k) increases as light power is decreased and eventually saturates when the power becomes small enough, so does the difference between the k with and without gate bias (inset of Fig. S8-1). At the wavelength of 4°μm, the modulation depth increases from ~1 dB under microwatt power and saturates at ~11 dB when the power is below nanowatt (Fig. S8-1). The modulation strength could be further improved by reducing the thickness of the gate dielectric, and using a thinner (~10 nm) BP to eliminate the screening effects while maintaining the bulk bandgap. The higher modulation efficiency under lower light power indicates the device's potential for processing weak signal in a noisy background, which is vital to applications such as biomedical imaging and trace gas detection. Among the integrated modulators for mid-infrared, our work achieved the most compact footprint of 225 μm

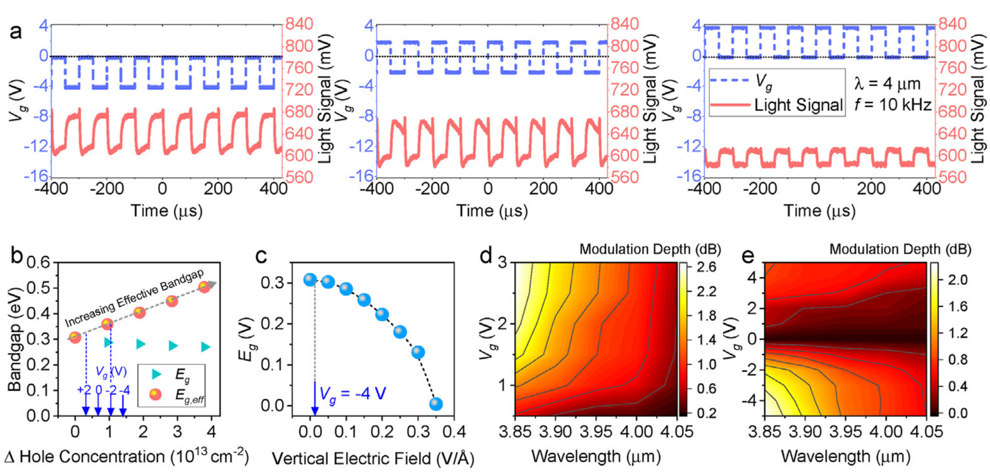

Fig. 3. (a) Gate bias (V_g) and corresponding modulated light signal in time domain under a modulation frequency of 10 kHz. V_g with the same magnitude of change is applied in three different ways [green (V_g: 4–0 V), orange (V_g: −2 to +2 V) and pink (V_g: 0 to +4 V) curves]. Wavelength = 4 μm. The distinct responses of light signal under different V_g regimes could be explained by DFT calculations for (b) Burstein−Moss effect (band filling effect vs. hole concentration) and (c) Franz−Keldysh effect (bandgap vs. vertical electric field). Mappings of modulation depth against V_g and wavelength for (d) gate bias switching between $+|V_g|$ and $-|V_g|$ and (e) gate bias switching between 0 V and V_g, which agree well with theoretical calculations.

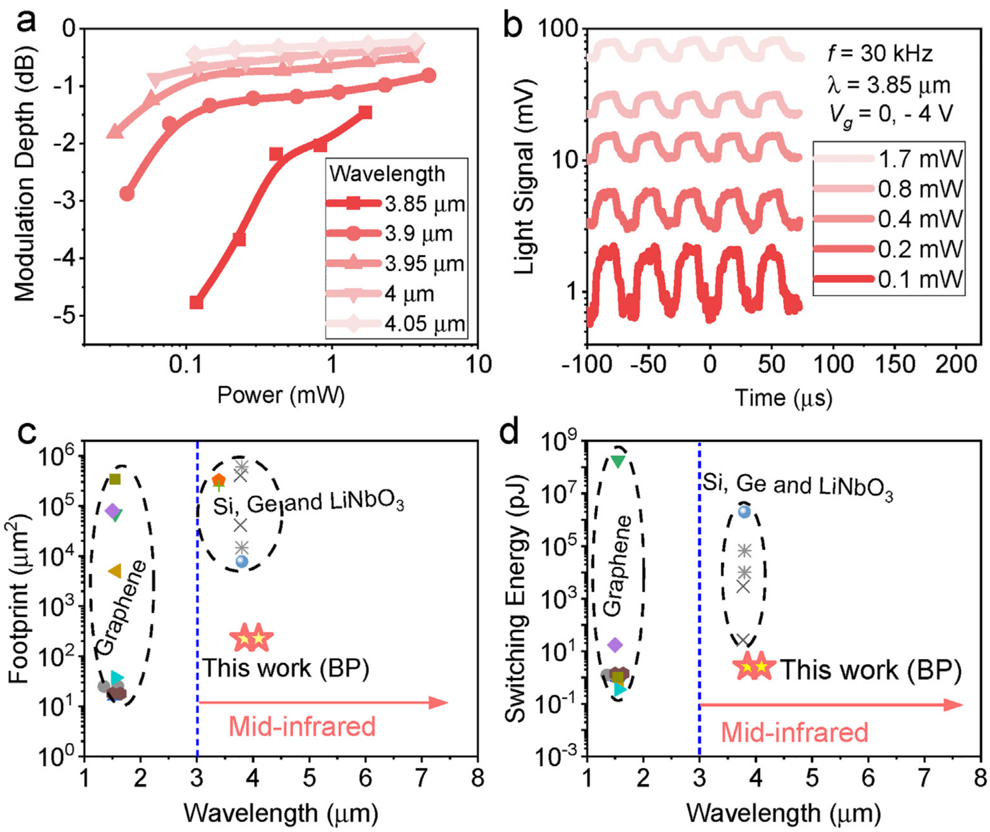

Fig. 4. (a) Modulation is more efficient under weaker light power for all the measured wavelengths, as evidenced by (b) a more pronounced extinction in the modulated light signal. Among the waveguide-integrated modulators for mid-infrared, our device has the smallest (c) footprint and lowest (d) switching energy.

[2] (Fig. 4c) and lowest switching energy (2.6 pJ) (Fig. 4d). A more detailed benchmarking is provided in Supporting Note 9.

The realisation of an on-chip mid-infrared system necessitates the co-integration of active components including photodetector and modulator. Fig. 1a exemplifies an application for chemical sensing. Arrays of photodetectors analyse the light after its interaction with the unknown chemical, meanwhile the modulators manipulate the light in each channel at a certain frequency so that

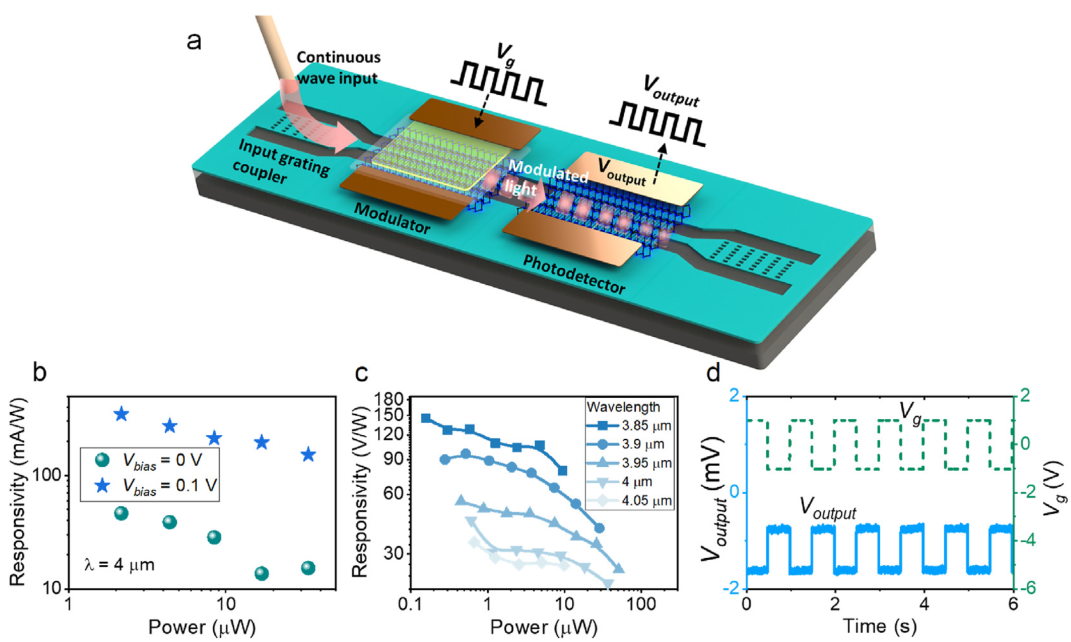

Fig. 5. (a) Illustrations of BP modulator and photodetector integrated on the same chip. Continuous wave is modulated while traveling through the waveguide underneath the BP modulator, then it is guided by the Si layer and received by the BP photodetector. (b) Current and (c) voltage responsivity of the photodetector. Power dependence due to saturable absorption is consistent with previous studies. Zero bias operation enables low standby power consumption. (d) Voltage output from BP photodetector as the gate bias on BP modulator switching between +1 and −1 V.

the signal could be differentiated from the noise. As a step further towards such applications, we integrated BP modulator and photodetector on the same chip (Fig. 5a). Under 0.1 V bias, the photodetector achieved a responsivity of ~0.3 A/W at 4 μm (Fig. 5b). It is worth noting that a small bias could lead to a huge dark current in the photodetector (Fig. S10-2) due to the large channel width that resulted from the waveguide integration. However, zero bias operation is enabled by the asymmetric electrode layout in our photodetector (Fig. S10-6d). This could significantly reduce the dark current and the standby power consumption in the photodetector while achieving a current responsivity of ~40 mA/W (Fig. 5b) and a voltage responsivity up to 44 V/W (Figs. 5c, 4 μm). With ± V gate bias applied to the modulator, the open circuit voltage in the photodetector due to photovoltaic effect could be switched between two levels (Fig. 5d). Our integration suggests the fabrication compatibility among different active components as they were completed using the same process flow, and also verifies the functional diversification of the BP/Si photonic platform. Nevertheless, further characterisations (Supporting Note 10) indicate the presence of an electrical interference between the photodetector and the modulator, which requires further efforts to improve the electrical isolation. Implementing an adequate oxide cladding using a standardised fabrication process could potentially offer a solution to overcoming such issue. With recent development on BP material growth with property control [23,39–43], we could expect such integration to be realised in larger scale and even towards commercialisation.

3. Conclusions

In conclusion, the strategy of integrating BP photonics and Si photonics for realising optic modulators manifests a cornerstone for the development of a fully integrated on-chip system for mid-infrared applications. The anisotropic modulation of BP's optical properties and the integration with Si waveguide plays a critical role in optimising the light–BP interaction, which contributes to a much more pronounced modulation depth at a small gate bias, indicating superior competence for weak light conditions. Leveraging on the waveguide design, a compact active footprint and a remarkably lower power consumption than conventional modulators based on three-dimensional materials are demonstrated. The significance of this work is not only achieving superior device performance, but also addressing the material compatibility issues that have plagued the development of a fully integrated mid-infrared system. The co-integration of a hybrid BP-Si photonics using facile CMOS (complementary metal-oxide-semiconductor) fabrication process holds great potential to enable functional diversification of optoelectronic chips for various practical applications such as on-chip bio-sensing, night vision, and food inspection.

4. Methods

4.1. Fabrication and characterisation of the surface-illuminated sample for FTIR measurements

BP flakes were exfoliated to a stamp from bulk crystal (smart elements) by tape. The 40-nm thick (measured by atomic force microscope) flake with lateral size of ~100 μm by 100 μm was transferred onto the CaF_2 substrate. The ground electrode was patterned by laser writer (Microtech LW405B) with AZ1512HS as the photoresist, followed by Ni/Au (6/60 nm) deposition by sputtering. The BP flake with a ground electrode was covered with 30-nm Al_2O_3 deposited by atomic layer deposition (ALD) as the top gate dielectric layer. To minimise the resistance of the gate electrode, the 20-nm ITO (deposited by sputtering) was connected to a metal (6/60 nm Ni/Au) pad for probing. Raman spectroscopy (WITec Alpha 300R) was used to identify the crystal orientation of the BP flake, as labelled in the microscope image (Fig. S3-1a). The FTIR spectra were measured by Agilent Cary 600 Spectrometer.

4.2. Fabrication and characterisation of the waveguide-integrated modulator

Starting from the SOI substrate, electron beam lithography (EBL) (Joel EBL, JBX-6300FS) was used for Si photonic layer patterning with ZEP 520A as the e-beam resist. The pattern was then transferred from the resist to the Si layer by fluorine-based deep reactive ion etching. After the etching, the ZEP 520A resist was removed by Remover PG (MicroChem) with ultrasonic bath, followed by isopropyl alcohol rinse. The layer of 18-nm Al_2O_3 for insulation and adhesion was grown on the Si photonic layer by ALD. BP flakes were exfoliated onto a transparent stamp (Gel-Pak, PF-20/17-X4) from bulk crystal by tape. Then the BP flake with desired thickness (20 nm) and lateral size was selected under an optic microscope. Polarisation-resolved Raman spectroscopy with 532-nm laser was measured to identify the crystal orientation of the selected BP flake. Using a micromanipulator under a microscope, the armchair orientation of the BP flake was aligned to the TE direction of the waveguide, after which the flake was transferred from the stamp onto the waveguide with SWG. The ground electrode was patterned by laser writer (Microtech LW405B) with AZ1512HS as the photoresist. The 6-nm Ni and 60-nm Au were deposited by sputtering as metal contact. After the lift-off for the ground electrode, 30-nm Al_2O_3 gate dielectric was deposited by ALD at 120°C. Then the ITO top-gate and metal pad (6/60-nm Ni/Au) were patterned by laser writer and deposited by sputtering, completing the fabrication process. The light source was a continuous wave laser (Daylight Solutions Inc., TLS-41038). Modulated light was coupled out from the chip into an optical fibre connected to a photodetector (Thorlabs, PDAVJ5 at gain 8). The input electrical signal from a function generator (Keysight DSOX1102G) and the output signal from the photodetector were collected by an oscilloscope (Keysight DSOX3034A). The frequency response was measured by a network analyser (Agilent 4395A).

Data availability

The data that support the plots within this article and other findings of this study are available from the corresponding author upon reasonable request.

Author contributions

Li Huang: Conceptualisation, Methodology, Writing – original draft. Bowei Dong: Software, Methodology. Zhi Gen Yu: Software. Jingkai Zhou: Methodology. Yiming Ma: Methodology. Yong-Wei Zhang: Writing – review & editing. Chengkuo Lee: Writing – review & editing. Kah-Wee Ang: Supervision, Conceptualisation, Writing – review & editing.

Declaration of competing interest

The authors declare that they have no known competing financial interests or personal relationships that could have appeared to influence the work reported in this paper.

Acknowledgements

This research is supported by the A*STAR Science and Engineering Research Council (No. 152-70-00013) and by the National

Research Foundation under its Competitive Research Programs (NRF-CRP15-2015-01 and NRF-CRP15-2015-02).

Appendix A. Supplementary data

Supplementary data to this article can be found online at https://doi.org/10.1016/j.mtadv.2021.100170.

References

[1] R. Soref, Group IV photonics for the mid infrared, Proc. SPIE, in: Silicon Photonics VIII, vol. 8629, 2013, 862902-862901.
[2] R. Soref, Mid-infrared photonics in silicon and germanium, Nat. Photonics 4 (2010) 495–497.
[3] D. Rodrigo, O. Limaj, D. Janner, D. Etezadi, F.J. Garcia de Abajo, V. Pruneri, H. Altug, Mid-infrared plasmonic biosensing with graphene, Science 349 (2015) 165–168.
[4] G. Marriott, S. Mao, T. Sakata, J. Ran, D.K. Jackson, C. Petchprayoon, T.J. Gomez, E. Warp, O. Tulyathan, H.L. Aaron, E.Y. Isacoff, Y. Yan, Optical lock-in detection imaging microscopy for contrast-enhanced imaging in living cells, Proc. Natl. Acad. Sci. U. S. A. 105 (2008) 17789–17794.
[5] G.T. Reed, G. Mashanovich, F.Y. Gardes, D.J. Thomson, Silicon optical modulators, Nat. Photonics 4 (2010) 518–526.
[6] M.J.R. Heck, Highly integrated optical phased arrays: photonic integrated circuits for optical beam shaping and beam steering, Nanophotonics 6 (2017) 93–107.
[7] R.A. Becker, R.H. Rediker, T.A. Lind, Wide-bandwidth guided-wave electro-optic intensity modulator at λ=3.39 μm, Appl. Phys. Lett. 46 (1985) 809–811.
[8] J. Chiles, S. Fathpour, Mid-infrared integrated waveguide modulators based on silicon-on-lithium-niobate photonics, Optica 1 (2014) 350–355.
[9] A. Malik, S. Dwivedi, L. Van Landschoot, M. Muneeb, Y. Shimura, G. Lepage, J. Van Campenhout, W. Vanherle, T. Van Opstal, R. Loo, G. Roelkens, Ge-on-Si and Ge-on-SOI thermo-optic phase shifters for the mid-infrared, Opt Express 22 (2014) 28479–28488.
[10] M. Nedeljkovic, S. Stankovic, C.J. Mitchell, A.Z. Khokhar, S.A. Reynolds, D.J. Thomson, F.Y. Gardes, C.G. Littlejohns, G.T. Reed, G.Z. Mashanovich, Mid-infrared thermo-optic modulators in SoI, IEEE Photon. Technol. Lett. 26 (2014) 1352–1355.
[11] M. Nedeljkovic, C.G. Littlejohns, A.Z. Khokhar, M. Banakar, W. Cao, J.S. Penades, D.T. Tran, F.Y. Gardes, D.J. Thomson, G.T. Reed, H. Wang, G.Z. Mashanovich, Silicon-on-insulator free-carrier injection modulators for the mid-infrared, Opt. Lett. 44 (2019) 915–918.
[12] T. Li, M. Nedeljkovic, N. Hattasan, W. Cao, Z. Qu, C.G. Littlejohns, J.S. Penades, L. Mastronardi, V. Mittal, D. Benedikovic, D.J. Thomson, F.Y. Gardes, H. Wu, Z. Zhou, G.Z. Mashanovich, Ge-on-Si modulators operating at mid-infrared wavelengths up to 8 μm, Photonics Res 7 (2019) 828–836.
[13] L. Huang, K.-W. Ang, Black phosphorus photonics toward on-chip applications, Appl. Phys. Rev. 7 (2020) 31302.
[14] L. Huang, B. Dong, X. Guo, Y. Chang, N. Chen, X. Huang, W. Liao, C. Zhu, H. Wang, C. Lee, K.-W. Ang, Waveguide-integrated black phosphorus photodetector for mid-infrared applications, ACS Nano 13 (2019) 913–921.
[15] R. Peng, K. Khaliji, N. Youngblood, R. Grassi, T. Low, M. Li, Midinfrared electro-optic modulation in few-layer black phosphorus, Nano Lett. 17 (2017) 6315–6320.
[16] C. Chen, F. Chen, X. Chen, B. Deng, B. Eng, D. Jung, Q. Guo, S. Yuan, K. Watanabe, T. Taniguchi, M.L. Lee, F. Xia, Bright mid-infrared photoluminescence from thin-film black phosphorus, Nano Lett. 19 (2019) 1488–1493.
[17] C. Chen, X. Lu, B. Deng, X. Chen, Q. Guo, C. Li, C. Ma, S. Yuan, E. Sung, K. Watanabe, T. Taniguchi, L. Yang, F. Xia, Widely tunable mid-infrared light emission in thin-film black phosphorus, Sci. Adv. 6 (2020).
[18] Y. Huang, J. Ning, H. Chen, Y. Xu, X. Wang, X. Ge, C. Jiang, X. Zhang, J. Zhang, Y. Peng, Z. Huang, Y. Ning, K. Zhang, Z. Zhang, Mid-infrared black phosphorus surface-emitting laser with an open microcavity, ACS Photonics 6 (2019) 1581–1586.
[19] J. Wang, A. Rousseau, M. Yang, T. Low, S. Francoeur, S. Kéna-Cohen, Mid-infrared polarized emission from black phosphorus light-emitting diodes, Nano Lett. 20 (2020) 3651–3655.
[20] Y. Zhang, S. Wang, S. Chen, Q. Zhang, X. Wang, X. Zhu, X. Zhang, X. Xu, T. Yang, M. He, X. Yang, Z. Li, X. Chen, M. Wu, Y. Lu, R. Ma, W. Lu, A. Pan, Wavelength-tunable mid-infrared lasing from black phosphorus nanosheets, Adv. Mater. (2020), e1808319.
[21] X. Ling, H. Wang, S. Huang, F. Xia, M.S. Dresselhaus, The renaissance of black phosphorus, Proc. Natl. Acad. Sci. U. S. A. 112 (2015) 4523–4530.
[22] B. Guo, Q.l. Xiao, S.h. Wang, H. Zhang, 2D layered materials: synthesis, nonlinear optical properties, and device applications, Laser Photon. Rev. 13 (2019) 1800327.
[23] X. Li, B. Deng, X. Wang, S. Chen, M. Vaisman, S.-i. Karato, G. Pan, M. Larry Lee, J. Cha, H. Wang, F. Xia, Synthesis of thin-film black phosphorus on a flexible substrate, 2D Mater. 2 (2015) 31002.
[24] S. Deckoff-Jones, H. Lin, D. Kita, H. Zheng, D. Li, W. Zhang, J. Hu, Chalcogenide glass waveguide-integrated black phosphorus mid-infrared photodetectors, J. Opt. 20 (2018) 44004.
[25] J. Bullock, M. Amani, J. Cho, Y.-Z. Chen, G.H. Ahn, V. Adinolfi, V.R. Shrestha, Y. Gao, K.B. Crozier, Y.-L. Chueh, A. Javey, Polarization-resolved black phosphorus/molybdenum disulfide mid-wave infrared photodiodes with high detectivity at room temperature, Nat. Photonics 12 (2018) 601–607.
[26] Y. Yin, R. Cao, J. Guo, C. Liu, J. Li, X. Feng, H. Wang, W. Du, A. Qadir, H. Zhang, Y. Ma, S. Gao, Y. Xu, Y. Shi, L. Tong, D. Dai, High-speed and high-responsivity hybrid silicon/black-phosphorus waveguide photodetectors at 2 μm, Laser Photon. Rev. 13 (2019) 1900032.
[27] N. Youngblood, C. Chen, S.J. Koester, M. Li, Waveguide-integrated black phosphorus photodetector with high responsivity and low dark current. Waveguide-integrated black phosphorus photodetector with high responsivity and low dark current, Nat. Photonics 9 (2015) 247–252.
[28] T.Y. Chang, Y. Chen, D.I. Luo, J.X. Li, P.L. Chen, S. Lee, Z. Fang, W.Q. Li, Y.Y. Zhang, M. Li, A. Majumdar, C.H. Liu, Black phosphorus mid-infrared light-emitting diodes integrated with silicon photonic waveguides, Nano Lett. 20 (2020) 6824–6830.
[29] T. Low, A.S. Rodin, A. Carvalho, Y. Jiang, H. Wang, F. Xia, A.H. Castro Neto, Tunable optical properties of multilayer black phosphorus thin films, Phys. Rev. B 90 (2014) 75434.
[30] C. Lin, R. Grassi, T. Low, A.S. Helmy, Multilayer black phosphorus as a versatile mid-infrared electro-optic Material, Nano Lett. 16 (2016) 1683–1689.
[31] W.S. Whitney, M.C. Sherrott, D. Jariwala, W.H. Lin, H.A. Bechtel, G.R. Rossman, H.A. Atwater, Field effect optoelectronic modulation of quantum-confined carriers in black phosphorus, Nano Lett. 17 (2017) 78–84.
[32] B. Deng, V. Tran, Y. Xie, H. Jiang, C. Li, Q. Guo, X. Wang, H. Tian, S.J. Koester, H. Wang, J.J. Cha, Q. Xia, L. Yang, F. Xia, Efficient electrical control of thin-film black phosphorus bandgap, Nat. Commun. 8 (2017) 14474.
[33] X. Chen, X. Lu, B. Deng, O. Sinai, Y. Shao, C. Li, S. Yuan, V. Tran, K. Watanabe, T. Taniguchi, D. Naveh, L. Yang, F. Xia, Widely tunable black phosphorus mid-infrared photodetector, Nat. Commun. 8 (2017) 1672.
[34] Y. Liu, Z. Qiu, A. Carvalho, Y. Bao, H. Xu, S.J. Tan, W. Liu, A.H. Castro Neto, K.P. Loh, J. Lu, Gate-tunable giant Stark effect in few-layer black phosphorus, Nano Lett. 17 (2017) 1970–1977.
[35] M.C. Sherrott, W.S. Whitney, D. Jariwala, S. Biswas, C.M. Went, J. Wong, G.R. Rossman, H.A. Atwater, Anisotropic quantum well electro-optics in few-layer black phosphorus, Nano Lett. 19 (2019) 269–276.
[36] B. Liu, M. Kopf, A.N. Abbas, X. Wang, Q. Guo, Y. Jia, F. Xia, R. Weihrich, F. Bachhuber, F. Pielnhofer, H. Wang, R. Dhall, S.B. Cronin, M. Ge, X. Fang, T. Nilges, C. Zhou, Black arsenic-phosphorus: layered anisotropic infrared semiconductors with highly tunable compositions and properties, Adv. Mater. 27 (2015) 4423–4429.
[37] T.S. Moss, The interpretation of the properties of indium antimonide, Proc. Phys. Soc. B 67 (1954) 775–782.
[38] W. Franz, Einfluß eines elektrischen Feldes auf eine optische Absorptionskante, Z. Naturforsch. 13 (1958) 484–489.
[39] Y. Xu, X. Shi, Y. Zhang, H. Zhang, Q. Zhang, Z. Huang, X. Xu, J. Guo, H. Zhang, L. Sun, Z. Zeng, A. Pan, K. Zhang, Epitaxial nucleation and lateral growth of high-crystalline black phosphorus films on silicon, Nat. Commun. 11 (2020) 1330.
[40] J.B. Smith, D. Hagaman, H.F. Ji, Growth of 2D black phosphorus film from chemical vapor deposition, Nanotechnology 27 (2016) 215602.
[41] M. Liu, S. Feng, Y. Hou, S. Zhao, L. Tang, J. Liu, F. Wang, B. Liu, High yield growth and doping of black phosphorus with tunable electronic properties, Mater. Today 36 (2020) 91–101.
[42] Z. Wu, Y. Lyu, Y. Zhang, R. Ding, B. Zheng, Z. Yang, S.P. Lau, X.H. Chen, J. Hao, Large-scale growth of few-layer two-dimensional black phosphorus, Nat. Mater. 20 (2021) 1203–1209.
[43] C. Li, Y. Wu, B. Deng, Y. Xie, Q. Guo, S. Yuan, X. Chen, M. Bhuiyan, Z. Wu, K. Watanabe, T. Taniguchi, H. Wang, J.J. Cha, M. Snure, Y. Fei, F. Xia, Synthesis of crystalline black phosphorus thin film on sapphire, Adv. Mater. 30 (2018) 1703748.